The trapping and release of bubbles from a linear pore

Geoffrey Dawson[1], Sungyon Lee[2] and Anne Juel[1],†

[1]Manchester Centre for Nonlinear Dynamics and School of Mathematics, University of Manchester, Manchester M13 9PL, UK

[2]UCLA Mathematics Department, Box 951555, Los Angeles, CA 90095-1555, USA

Streamwise variation in vessel geometry is a feature of many multiphase flows of practical interest, ranging from natural porous media flows to man-made lab-on-the-chip applications. The variable streamwise geometry typically exerts a dominant influence on bubble motion, and can lead to undesirable phenomena such as clogging of the vessel. Here, we study clogging in a fundamental configuration, where a tube of square cross-section is suddenly expanded over a short streamwise distance. The extent to which a bubble driven by constant flux flow broadens to partially fill the expansion depends on the balance between viscous and surface tension stresses, measured by the capillary number Ca. This broadening is accompanied by the slowing and momentary arrest of the bubble as Ca is reduced towards its critical value for trapping. For $Ca < Ca_c$ the pressure drag forces on the quasi-arrested bubble are insufficient to force the bubble out of the expanded region so it remains trapped. We examine the conditions for trapping by varying bubble volume, flow rate of the carrier fluid, relative influence of gravity and length of expanded region. We find specifically that Ca_c depends non-monotonically on the size of the bubble. We verify, with experiments and a capillary static model, that a bubble is released if the work of the pressure forces over the length of the trap exceeds the surface energy required for the trapped bubble to reenter the constricted square tube.

Key words: capillary flows, drops and bubbles, microfluidics

1. Introduction

Multiphase flows of practical interest are characterized by complex vessel geometries, with examples ranging from natural porous media to man-made lab-on-a-chip devices. Models based on the over-simplification of the pore geometry have been shown to suppress fundamental physical behaviour. For example, a tube whose local flow resistance varies across its cross-section can support multiple types of propagating bubbles associated with widely different liquid recovery rates (de Lózar *et al.* 2009), as well as periodically deforming bubbles (Pailha *et al.* 2012), by contrast to the unique family of bubbles associated with circular or square tube cross-sections

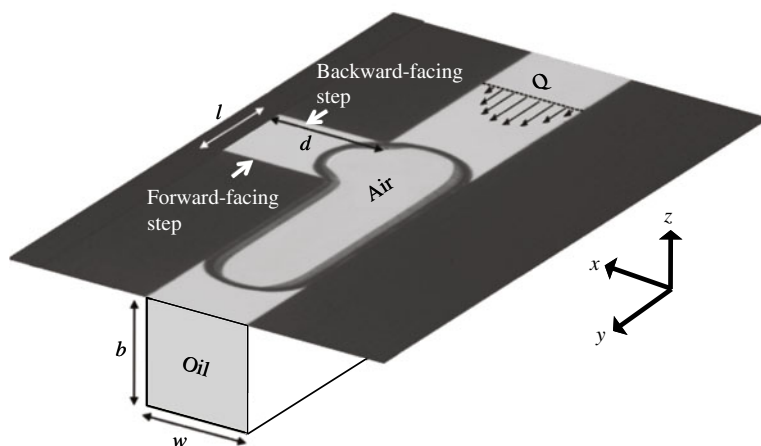† Email address for correspondence: anne.juel@manchester.ac.uk

FIGURE 1. A three-dimensional view of a square channel of depth b and width w, with a pair of forward and backward facing steps forming an expansion of length, l and width d. An air bubble (in top view) is trapped in the expansion under imposed constant volume-flux flow of oil, Q. We define a Cartesian coordinate system (xyz), with y parallel to the flow direction and z antiparallel to the acceleration of gravity.

(Hazel & Heil 2002). Streamwise variations of the tube geometry in the form of smooth or sudden constrictions, or alternatively enlargements of the tube cross-section, can equally exert a dominant influence on the motion of bubbles or droplets by generating displacement and reconfiguration of drops or bubbles (Renvoisé *et al.* 2009), controlling droplet formation (Amyot & Plouraboué 2007), facilitating bubble sorting (Tan *et al.* 2004), synchronizing droplet motion (Ahn *et al.* 2011), but also disturbing the functionality of microfluidic devices through clogging (Jensen, Goranovi & Bruus 2004) and reducing the quality of fibre-based composites through bubble trapping (Lundström 1996).

We study the effect on bubble motion of a sudden streamwise expansion of a tube of square cross-section, which is formed by a pair of backward-facing and forward-facing steps as shown in figure 1. This simple geometry models a pore with a connectivity of two and we focus on the conditions necessary for clogging. The trapping of bubbles in a tube relies on the fact that a static bubble large enough to span the entire tube cross-section is geometrically constrained to adopt an elongated shape, which increases its surface energy compared with its relaxed spherical configuration. Hence, it will tend to reduce its confinement upon expansion of the tube cross-section to release surface energy. Under constant-flux flow with negligible inertial forces, the bubble configuration is primarily governed by the capillary number $Ca = \mu Q/(A\sigma)$, which is a measure of the ratio of viscous to surface tension forces, where Q is the flow rate, $A = bw$ the cross-sectional area of the tube, and μ and σ are the dynamic viscosity and the surface tension of the carrier fluid, respectively. The strength of the viscous forces on the capillary scale determines the level of broadening of the bubble upon dynamic encounter of a channel expansion, as well as the ability of the bubble to squeeze into a contraction of the tube, with small values of Ca facilitating the trapping of bubbles in expanded sections of the tube.

Studies of microchannel clogging by bubbles have focused on slowly varying cross-sections and quasi-static bubbles, because of the complexity of modelling the

dynamics of the liquid–gas, liquid–solid and solid–gas interfaces as well as the dynamics in the bulk fluids. Jensen *et al.* (2004) predicted the clogging pressure required to mobilize a wetting bubble depending on taper angle. Good agreement with direct pressure measurements was found at low *Ca*, but deviations due to viscous flow effects were measured for $Ca > 10^{-1}$ (Chio *et al.* 2006). Moreover, they identified a small range of taper angles that could lead to a reduction in bubble energy as it moved into the constriction. The critical capillary number required to mobilize a non-wetting bubble trapped in a long and smooth constriction of a two-dimensional tube under constant-flux flow was shown to decrease monotonically with bubble length by Legait (1983).

The generation of surface energy gradients due to expansions or contractions of the channel is useful as a design tool in microreactors, where droplets/cells need to be trapped and subsequently released after manipulation. Controlled merging of droplets has been demonstrated by pairing a sudden contraction with a bypass (Köhler *et al.* 2004). A similar design was exploited to store droplets (Boukellal *et al.* 2009), while Um & Park (2009) used a sinuous groove etched in the bottom boundary of the channel to guide drops into a widely expanded microchannel that enabled flow-rate-controlled merging of multiple droplets. The use of grooves etched in the top surface of a wide microchannel was further exploited by Abbyad *et al.* (2011) to guide or anchor drops against a mean flow for outer flow velocities below a critical value. The anchor mechanism was investigated by Dangla, Lee & Baroud (2011) for droplets of radius that were large compared with their anchor groove in a quasi-two-dimensional microchannel (also known as a Hele-Shaw cell). This enabled an essentially two-dimensional analysis of both the droplet shape and the constant flux outer flow, which was only partially obstructed by the presence of the trapped droplet. They found that droplets remain trapped if their gradient in surface energy exceeds the drag force from the outer flow.

The linear pore model shown in figure 1 is three-dimensional. A non-wetting bubble, which typically spans the entire tube cross-section, is transported by constant-flux flow of a wetting fluid towards the sudden expansion. We examine the conditions for trapping by varying bubble volume, flow rate of the carrier fluid and length of expanded region. Once trapped, the bubble clogs the entire tube cross-section except for small corner regions, and this 'leaky piston' configuration (Wong, Radke & Morris 1995*a*,*b*) leads to a significant pressure drag as the constant flux flow must squeeze through a much reduced cross-section imposed by the configuration of the obstructing bubble. Moreover, the bubble shape is strongly affected by buoyancy forces, which tend to deform it by pushing it upwards, eventually lifting the bubble off the bottom boundary, and hence reducing its cross-section for Bond numbers $Bo = \rho g b^2 / 4\sigma \simeq 1$, where ρ is the density of the carrier fluid, g the acceleration of gravity and Bo the ratio of buoyancy to surface tension forces (de Lózar, Juel & Hazel 2008). We consider two values of the Bond number, $Bo \simeq 1$ and $Bo \simeq 0$ by performing experiments in millimetric and micrometric tubes, respectively.

The experimental methods are described in § 2. In § 3, we investigate the efficiency of trapping as a function of bubble size and find a non-monotonic dependence on the bubble length of the critical capillary number below which a bubble is trapped. The critical capillary number reaches a maximum value for the smallest bubble volume that enables the broadened bubble to fill the entire length of the expansion. Trapping occurs at very low values of the capillary number, which are associated with extremely thin liquid films separating the bubble from the tube boundary, so that accurate numerical simulation of the three-dimensional free boundary Stokes problem

poses a considerable challenge (de Lózar *et al.* 2008). Instead, we calculate capillary static bubbles under gravity and streamwise pressure forces with Surface Evolver (Brakke 2008) in §4 and find that this simplified model captures the experimental trapped bubble shapes accurately. Although the initial conditions provided by the steady bubble motion upstream of the expansion select a unique type of experimental trapped bubble, we find evidence of other families of trapped bubble shapes by varying initial conditions both experimentally and in the static model. We verify in §5 with a combination of experiments and capillary static simulations that the work of the pressure forces on the bubble must exceed the change in surface energy of the bubble upon trapping in order for the bubble to be released, a criterion similar to that proposed by Dangla *et al.* (2011). Conclusions are presented in §6.

2. Experimental methods

The experiments were performed in both millimetric and micrometric tubes of square cross-section of width w and depth b with $w \simeq b$. Each tube included a sudden expansion of length l into one of its sidewalls, so that the width of the tube was increased to $w+d$ with a backward-facing step and returned to w with a forward-facing step as shown in figure 1. We chose $d \geqslant w$, in order for the bubble not to reach the bottom of the expansion. The experiments were performed with expansions of length equal to the width of the tube, i.e. $l/w = 1.0$ unless otherwise stated. The millimetric tube had cross-sectional dimensions $b \times w = (3.04 \pm 0.01) \times (3.00 \pm 0.07)$ mm. The top and bottom boundaries of the channel were made of float glass plates of a thickness of 2 cm, separated by steel gauge plates, which formed its sidewalls. The expansions were created by accurately positioning and attaching two rectangular pieces of the same gauge plate (60 mm × 12 mm) to one of the sidewalls separated by a distance l, to create the forward and backward facing steps. The dimensions of the microtube were $b \times w = (250 \pm 4) \times (250 \pm 4)$ µm. It was manufactured by micro-milling of a piece of Perspex (CAT3D-M6, CNC, milling machine, Datron Technologies Ltd), and sealed with a clear adhesive film (Corning), which was supported by a precision-milled flat Perspex lid. The millimetric and micrometric tubes had length/width ratios of 20 and 80, respectively.

Each tube was completely filled with a moderate viscosity liquid and connected to liquid reservoirs at both ends: we used silicone oil (polydimethylsiloxane from Basildon Chemicals Ltd, $\mu = 1.03 \times 10^{-2}$ kg m^{-1} s^{-1}, $\rho = 940$ kg m^{-3} and $\sigma = 20.1 \times 10^{-3}$ Nm^{-1}, at the laboratory temperature of $21 \pm 1\,^{\circ}$C) in the millimetric tube, and Galden$^{\text{TM}}$ HT135 (perfluoropolyether from Solvay Solexis, $\mu = 1.75 \times 10^{-3}$ kg m^{-1} s^{-1}, $\rho = 1752$ kg m^{-3} and $\sigma = 17 \times 10^{-3}$ Nm^{-1}, at the laboratory temperature of $21 \pm 1\,^{\circ}$C) in the microtube. A constant volume flux flow Q was imposed by withdrawing liquid at one end with a syringe pump (KDS210, KD Scientific). In order to study the trapping of bubbles in the expansion, individual bubbles of controlled volume had to be generated rather than bubble trains, where successive bubbles would dislodge their preceding neighbour from the trap. Single bubbles of known volume were formed near the inlet of the millimetric tube by injecting air through a capillary tube (of internal diameter of 1 mm) into a constant flux flow. Different bubble sizes were obtained by varying the background and injection flow rates controlled by syringe pumps, and the volume of each bubble was determined from the time taken by the growing bubble to pinch off from the tip of the capillary tube. In the microtube, single bubbles were formed at the junction of the main liquid-filled channel and a rectangular side channel of

dimensions (250×250) μm by manually injecting air into the side channel and controlling bubble pinch-off by tilting the apparatus. Although more advanced control methods would be required to generate a single drop of prescribed volume (He, Kuo & Chiu 2005; Xu & Attinger 2008; Gu *et al.* 2011), we were able to form single bubbles of unknown volume, which we parametrized by measuring their static length *L*. In order to ensure reproducibility, the bubble length was monitored following each trapping measurement, and found to remain constant to within 0.07 mm and 4 μm of its original value in the millimetric and micrometric tubes, respectively. This level of bubble size control was achieved by taking care not to degas the silicone oil and partially degassing the Galden^{TM} HT135 fluid, to reduce dissolution of the air bubble into the surrounding fluid.

The bubble volume was selected so that the bubble would fill the entire width of the tube, and adopt an elongated static shape of length $L \geqslant w$ in the square tube of cross-sectional area bw. The motion of the bubble corresponds to a two-phase displacement flow (Wong *et al.* 1995*a*; de Lózar *et al.* 2008), and the use of a non-wetting bubble (air) in a wetting carrier fluid means that the contact angle is approximately zero. Inertial forces are negligible relative to viscous forces, as the Reynolds number $Re = \mu U b / \rho < 0.02$. Hence, the flow is governed primarily by viscous forces, surface tension forces and buoyancy forces. We define a capillary number, $Ca = \mu Q / (bw\sigma)$, which corresponds to a non-dimensional measure of the flow rate imposed externally. In the limit of low *Ca* where we performed experiments, the bubble deforms very little from its static shape, so that the fraction of liquid around the bubble remains approximately constant. However, as *Ca* increases, a bubble of fixed volume elongates under the increased influence of viscous forces and the fraction of liquid around the bubble increases (de Lózar *et al.* 2008). The Bond number, $Bo = \rho g b^2 / 4\sigma$ is specific to the fluids and channel used. In the millimetric channel, $Bo = 1.06 \pm 0.01$ while in the microtube $Bo = (1.6 \pm 0.1) \times 10^{-2}$. A linear relationship was measured in the millimetric square tube between volume and static length *L* of non-spherical bubbles ($L/w > 1$), which confirms that static bubbles are all subject to similar confinement imposed by the Bond number irrespective of their volume. Hence, we choose hereafter to quantify the bubble size with its initial static length *L* rather than its volume.

The outer edge of the bubbles was visualized as a dark contour due to refraction at the air–oil interface of light from an electroluminescent sheet placed directly under each tube. Top-view images were taken with a CMOS digital camera (with an image resolution of 1280×1024 pixels at a frame rate of up to 7 f.p.s.). The camera was setup 400 mm above the millimetric channel to yield a resolution of 30 pixels mm^{-1} with a F2, 35 mm lens, while in the small channel, the same lens with a 60 mm extension tube positioned 20 mm above the channel gave a resolution of 270 pixels mm^{-1}. The outer edge of the bubble was detected by locating a change in light intensity above a fixed threshold, using MATLAB's 'canny' edge detector.

We also performed pressure measurements at equal distances upstream and downstream of the expansion in the micrometric channel, as shown schematically in figure 2. Two identical channels of cross-sectional dimensions depth $\times$ width $=$ 250 μm $\times$ 100 μm, perpendicular to the main channel, were each connected to the 'wet' outlet of a differential ultralow pressure sensor (pressure range ± 625 Pa, Honeywell), while the 'dry' outlets were both placed in a controlled atmosphere. The same length of connecting tubing was used for both sensors to minimize systematic errors in the pressure readings. Both pressure sensors were calibrated with a column of HT135 over their entire range of operation, and the pressures measured with the sensor deviated
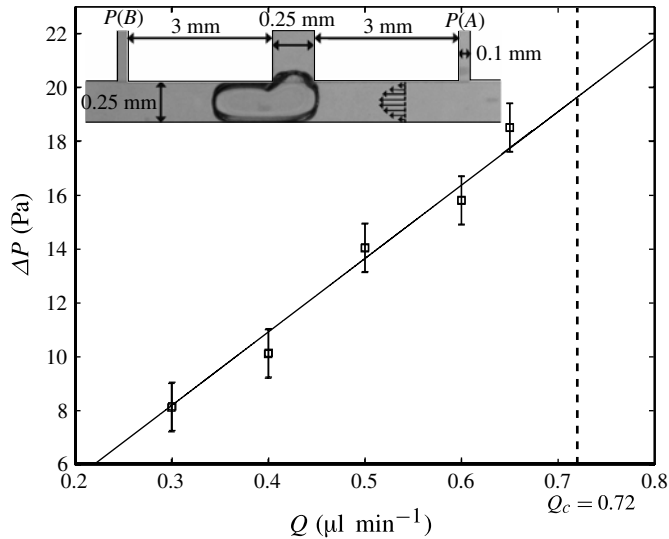
FIGURE 2. Variation of the pressure difference $\Delta P = P(A) - P(B)$ with flow rate Q ($\square$), when a bubble of length $L/w = 2.23$ is trapped in the expansion of the microtube. Here Q_c represents the threshold value beyond which the bubble is released from the expansion. The pressure was measured at points (A) and (B), respectively, using two Honeywell ultralow pressure sensors (pressure range of ± 625 Pa), to give an accurate measure of the pressure drop between the tail and the tip of a trapped bubble. A least-squares linear fit to the data of the form $\Delta P w / \sigma = \alpha_P Ca$ yields $\alpha_P = 13\,040 \pm 270$ (solid line), where $Ca = \mu Q / (\sigma b w)$.

from the linear calibration curve by a standard deviation of ± 1.4 Pa. Both sensors were used to measure pressures within the range (100–200 Pa), but the measured differential pressures were in the range (10–30 Pa). When a bubble was trapped in the expansion under constant flux flow, the difference in pressure between the two measuring points remained constant to within ± 1 Pa. The maximum pressure drop over this distance due to single phase Poiseuille flow through the square microtube was estimated to be 0.07 Pa, i.e. less than measurement noise. Thus, the recorded pressure difference gave an accurate measure of the pressure drop between the tail and the tip of the bubble. An example of the variation of this pressure drop with flow rate Q is shown in figure 2, which indicates proportionality between bubble pressure drop and flow rate and we refer to § 3 for further discussion of this result.

3. Trapping and release of bubbles

When a bubble travelling under constant volume flux forcing reaches the backward-facing step that marks the start of the expansion, the extent to which it broadens to partially fill the expansion depends on the balance between viscous stresses that drive the bubble forward and surface tension stresses that promote broadening, of which a measure is provided by the bubble capillary number $Ca = \mu Q / (bw\sigma)$.

A bubble of finite volume, and of an initial length L greater than the width of the tube ($L/w > 1$), can become trapped because it releases surface energy upon broadening into the expansion, and the energy deficit has to be overcome in order for the bubble to be forced back into the tube. As the value of Ca decreases, viscous forces due to the constant flux flow become insufficient to force the bubble over

the forward-facing step that marks the end of the expansion. Hence, the bubble gets trapped at a threshold value of the capillary number, $Ca_c > 0$ (see movies 1 and 2 in the online supplementary material available at http://dx.doi.org/10.1017/jfm.2013.103, showing the dynamics of the trapping process for values of Ca just above and below this threshold, respectively). A bubble trapped in the expansion is akin to a 'leaky piston' in that it typically occludes the majority of the square cross-section of the tube leaving only thin liquid films on the surfaces, except in small corner regions (Wong *et al.* 1995*a*) and in a thin region at the bottom of the tube when $Bo = 1.06$, because the bubble lifts off the bottom of the tube due to buoyancy (de Lózar *et al.* 2008).

When a finite bubble is in motion in a tube of square cross-section, the flow bypassing the bubble in the corner regions is small compared with the flow pushing the bubble, which is 30–100 times greater than the corner flow when neglecting the effects of gravity (Wong *et al.* 1995*b*). When the bubble is trapped, the totality of the constant volume-flux flow has to bypass the bubble, hence generating significant drag forces. In the case of a bubble, which has a stress-free interface, all the fluid bypassing the bubble contributes to a pressure drag, which builds up a pressure difference between the tail and the tip of the bubble. In the case of a large droplet confined in a Hele-Shaw cell, Dangla *et al.* (2011) showed that the contribution from viscous drag due to shear forces at the interface is negligible compared to the pressure drag. Moreover, heat losses may arise from viscous friction in very thin films, but we show in §5 that this effect is negligible in our configuration.

A direct measurement of the pressure drag on trapped bubbles is shown in figure 3, where the proportionality coefficient α_P between dimensionless pressure, $\Delta P w / \sigma$, and dimensionless flow rate, Ca, is plotted as a function of L/w for initial bubble lengths in the range $1.8 \leqslant L/w \leqslant 3.5$, as the pressure difference was too small to resolve for shorter bubbles. The squares correspond to values of α_P obtained from a linear fit of pressure data for $Ca < Ca_c$ as described in figure 2. These measurements could not be extended to $L/w > 2.4$ because the decreasing flow rates required to trap bubbles limited the range of Ca over which pressure measurements could be made. However, single pressure measurements were taken for $L/w > 2.4$ at $Ca = 0.9Ca_c$, and the values of α_P obtained from each of these measurements are shown with circles. The coefficient α_P can be locally approximated by the least-squares fit $\alpha_P = \alpha(L - L_0)/w$, with $\alpha = (1.9 \pm 0.2) \times 10^4$ and $L_0/w = 1.5 \pm 0.2$. The value of α is large because the channel width rather than the length scale of the thin liquid region between bubble and channel is used in the non-dimensionalization, although the latter sets the scale of the pressure drop. The minimum bubble length L_0/w is similar to the length of the shortest bubble that fills the length of the expansion when trapped (see figure 6) and thus it is approximately formed of two contiguous end caps. The linear variation of $\Delta P w / \sigma = \alpha Ca(L - L_0)/w$ with L for $L > L_0$ shown in figure 3 suggests that these end caps do not contribute significantly to the pressure drop along the bubble, and that the pressure drag increases linearly with the length of the thin film regions. The dashed line illustrates an assumed variation of the pressure drop for the shortest bubbles that do not fill the entire length of the expansion when trapped, which must be small and tend to zero as L/w decreases towards 1.0. We refer to §4 for a comparison with the analytical prediction of α in the limit of very long bubbles, whose main body is significantly longer than the end caps of approximate length L_0.

In order to measure the threshold value of Ca below which bubbles remained trapped, we captured the slowing of the bubble tip that accompanies broadening into the expansion as Ca is reduced towards Ca_c, by measuring a residence time of the bubble in the expanded section, τ_T, as shown in figure 4(*a*). Here τ_T was defined
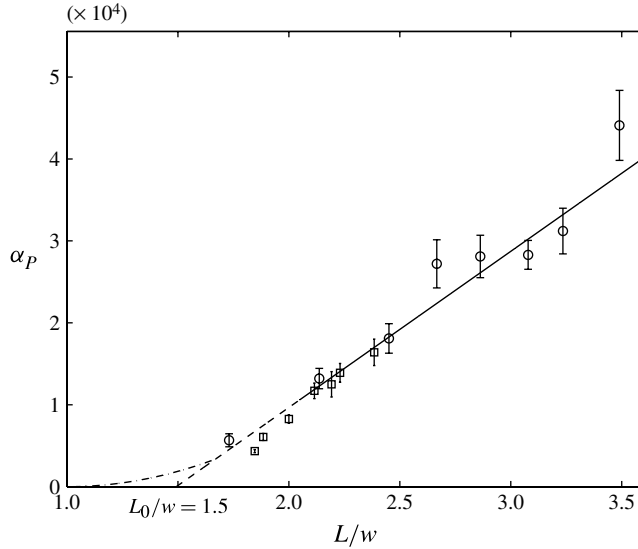
FIGURE 3. Variation of the proportionality coefficient α_P between pressure difference $\Delta Pw/\sigma$ and dimensionless flow rate Ca with initial bubble length L/w for bubbles trapped in the microtube where $w = 0.25$ mm: ($\square$) data obtained from linear fits to the bubble pressure drop as a function of flow rate when $Ca < Ca_c$ shown in figure 2; ($\bigcirc$) data obtained from single pressure drop measurements at $Ca = 0.9Ca_c$. The solid line is a linear least-squares fit of the form $\alpha_P = \alpha(L - L_0)/w$ where $\alpha = (1.9 \pm 0.2) \times 10^4$ and $L_0/w = 1.5 \pm 0.2$, which is extrapolated down to $\alpha_P = 0$ with a dashed line. The dashed-dotted line is a cubic extrapolation of the pressure coefficient to illustrate the fact that the pressure effectively only tends to zero as $L/w \to 1$.

as the time required for the bubble tip to advance from the backward-facing step that forms the start of the expansion at $y^* = -1/2$ to the bubble tail passing the forward-facing step that marks its end at $y^* = 1/2$, i.e. the time required for the tip to travel within $-1/2 \leqslant y_t^* \leqslant 1/2 + L/l$, where $y_t^* = y_t/l$ is dimensionless axial position of the tip. Periodic stick-slip motion of the syringe plungers caused a 1 and 2.5 % variation in bubble speed over a period of $20 < T_{osc} < 60$ s and $12 < T_{osc} < 40$ s in the millimetric and micrometric channels, respectively. This limited the accuracy on the value of Ca, leading to deviations of τ_T near Ca_c found to occur when τ_T was of the same order as the period of oscillation, T_{osc}. Hence, measurements of trap and release times could only be resolved for $\tau_T < T_{osc}/2$. The increase of the trapping time for decreasing dimensionless flow rates is illustrated in the inset of figure 4(b) for a bubble of length $L/w = 3.07$ in the millimetric tube. As Ca decreases, the tip position versus time curves develop a quasi-constant region, indicating the temporary arrest of the bubble in the expansion. The variation of the trapping time with Ca, shown in figure 4(b), is accurately represented by a hyperbolic three-parameter fit of the form $\tau_T = A/(Ca - Ca_c) + B$, where $Ca_c = (1.8 \pm 0.1) \times 10^{-4}$ is the maximum value of the capillary number at which the bubble will get trapped. The divergence of τ_T suggests critical slowing down near the trapping threshold and hence a loss of stability of the trapped bubble.

In support of this finding, we tested the stability of an initially trapped (and, hence, static) bubble, by switching the dimensionless flow rate from $Ca = 0$ to a value
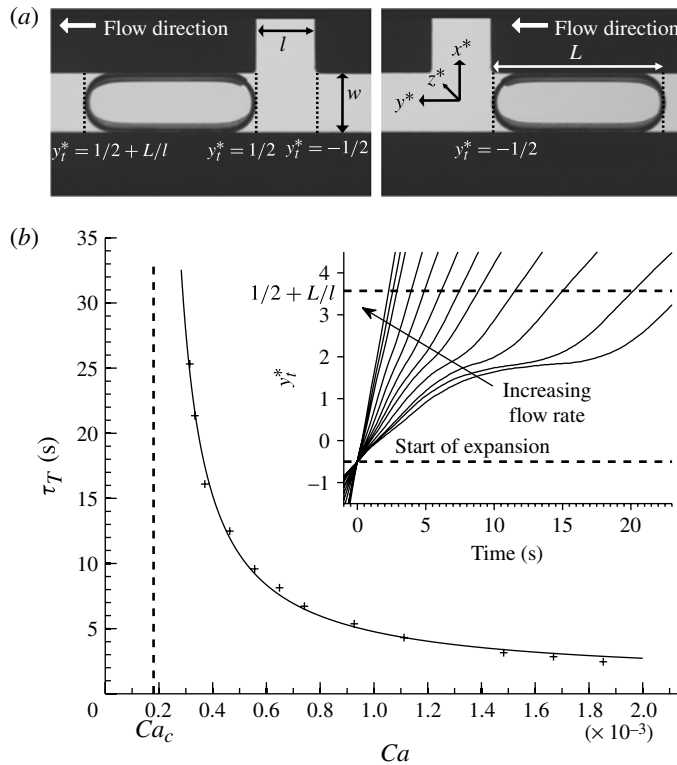
FIGURE 4. (a) Schematic diagram illustrating the measurement of the trapping time τ_T. This is the time taken by an initially moving bubble to travel through the expanded section of tube, with $-1/2 \leqslant y_t^* \leqslant 1/2 + L/l$, where $y_t^* = y_t/l$ is the dimensionless position of the bubble tip and $y_t^* = 1/2 + L/l$ is the tip position at which the tail of the bubble exits the expansion. (b) Variation of τ_T (+) with dimensionless flow rate Ca in the millimetric tube ($l = w = 3.0$ mm) for a bubble of dimensionless length $L/w = 3.07$. The solid line is a three-parameter hyperbolic fit of the form $\tau_T = A/(Ca - Ca_c) + B$, with $Ca_c = (1.8 \pm 0.1) \times 10^{-4}$, $A = (3.0 \pm 0.3) \times 10^{-3}$ s and $B = (1.1 \pm 0.5)$ s. Inset: dimensionless position of the bubble tip as a function of time.

above threshold, and measuring the time taken for the bubble to escape the trap. A comparison between the variation of trapping and release times with Ca is shown in figure 5 for bubbles of similar sizes in the microtube. Trapping times were measured for bubbles advancing through the expanded section of tube at $Ca > Ca_c$, while release times, τ_R, were measured from the instant the flow rate was switched to $Ca > Ca_c$ until the tail of the bubble passed the forward facing step, i.e. $y_t^* = 1/2 + L/l$. When starting the experiment with a trapped bubble, the initial tip position at $t = 0$ already exceeded the length of the expansion ($y_t^* > 1/2$), as shown in the inset of figure 5(b). The dependence of the tip position on time is similar in the insets of figure 5(a,b), with a region for $1.5 < y_t^* < 2.5$ where the tip temporarily arrests for increasing time intervals as Ca is reduced towards its threshold value. This suggests that trapping and release times are similar measures of the dynamics of trapping, as they both exhibit similar critical slowing down of the bubble passing through the expanded section of tube. The threshold values of the dimensionless flow rate obtained by hyperbolic fits of the trapping and release times were $Ca_c = (1.04 \pm 0.40) \times 10^{-5}$ for a bubble
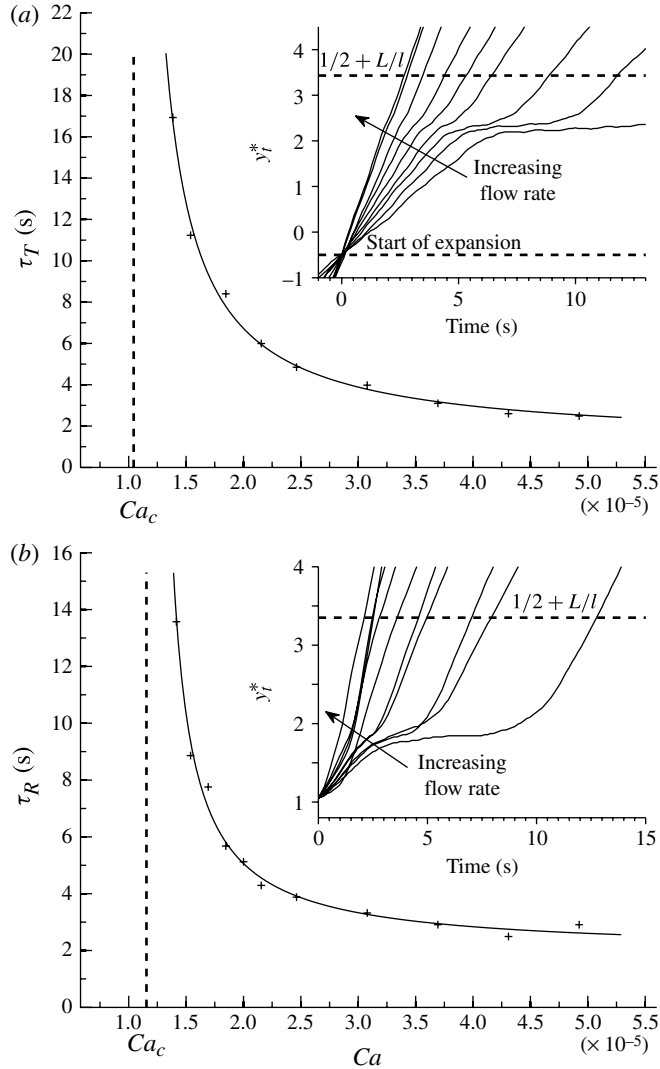
FIGURE 5. Dependence of trapping and release times ($+$) on dimensionless flow rate Ca in the micrometric tube ($l = w = 0.25$ mm). The solid line is a three-parameter hyperbolic fit of the form $A/(Ca - Ca_c) + B$. Inset: dimensionless position of the bubble tip as a function of time. (a) Trapping time τ_T for a bubble of dimensionless length $L/w = 2.93$. Fit parameters: $Ca_c = (1.04 \pm 0.40) \times 10^{-5}$, $A = (5.3 \pm 0.7) \times 10^{-5}$ s and $B = (1.2 \pm 0.4)$ s. (b) Release time τ_R taken by an initially trapped bubble to move through the expansion, for a bubble of dimensionless length $L/w = 2.85$. The measurement starts at the change in flow rate from an initial tip position $y_t^* > 1/2$, and ends when the tip reaches $y_t^* = 1/2 + L/l$. Fit parameters: $Ca_c = (1.15 \pm 0.10) \times 10^{-5}$, $A = (2.5 \pm 0.3) \times 10^{-5}$ s and $B = (2.0 \pm 0.2)$ s.

of length $L/w = 2.93$ in figure 5(a) and $Ca_c = (1.15 \pm 0.10) \times 10^{-5}$ for a bubble of length $L/w = 2.85$ in figure 5(b), respectively. The values obtained from the two different measurements methods were in quantitative agreement, as far they were indistinguishable to within experimental resolution.
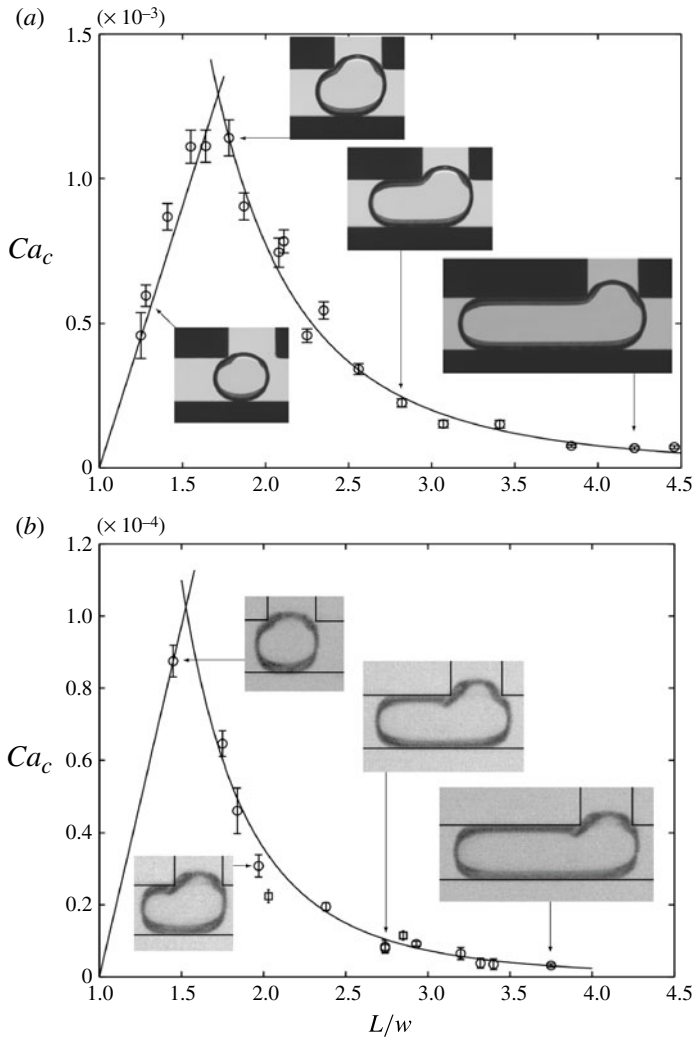
FIGURE 6. Variation of the dimensionless critical flow rate Ca_c with initial bubble length. Here Ca_c was extrapolated from either the trapping time distribution ($\bigcirc$) or the release time distribution of an initially trapped bubble τ_R ($\square$) (see figure 5). The error bars on Ca_c correspond to fitting uncertainties. The length of the most stable bubble, $(L/w)_{max}$, is estimated by approximating the increase in Ca_c at small initial bubble lengths by a linear dependence on length starting with $Ca_c = 0$ when $L/w = 1.0$, and the decrease at larger initial bubble length with a two parameter power fit of the form $L/w = ECa_c^F$, and calculating the intersection point between these curves. (a) Millimetric tube: $w = l = 3.0$ mm and $(L/w)_{max} = 1.71 \pm 0.08$; (b) microtube: $w = l = 0.25$ mm and $(L/w)_{max} = 1.52 \pm 0.14$.

The measurements of trapping and release times shown in figures 4 and 5 were repeated for a wide range of initial bubble lengths and the resulting values of Ca_c are shown as a function of the initial bubble length in figure 6. The circles correspond to values of Ca_c obtained from trapping times, while the squares represent data obtained from release times. In both millimetric and micrometric tubes, the smallest bubble we were able to trap had a length of $L/w = 1.35$, because of the very small flow rates

Tube	B_0	Ca_{max}	$(L/w)_{max}$
Millimetric	1.06	$(1.3 \pm 0.1) \times 10^{-3}$	1.71 ± 0.08
Micrometric	1.6×10^{-2}	$(1.0 \pm 0.1) \times 10^{-4}$	1.52 ± 0.14

TABLE 1. Summary of trapping results for different Bond numbers. Ca_{max} is the critical capillary number of the most stable bubble and $(L/w)_{max}$ is the static length of this bubble in the unexpanded tube.

required for trapping and the difficulties in generating bubbles of prescribed volume in the microtube (see § 2). As L/w became large, the flow rates required for trapping decreased to a level where the effect of stick-slip in the syringes became significant and where background vibration affected the stability of trapped bubbles, particularly in the microtube.

The variation of Ca_c is non-monotonic, as shown in figure 6(a), where Ca_c increases with L/w when the bubble is short, i.e. it does not fill the length of the expansion when trapped, and decreases with L/w when the bubble is long, i.e. it exceeds the length of the expansion when trapped. The observed trend is consistent with the limit of $Ca_c = 0$ for $L/w = 1.0$, which indicates that a bubble with a volume smaller than that required for $L/w = 1.0$ cannot get trapped. In figure 6(b), there is only one short bubble, but this argument enables us to infer a similar trend. The increase in Ca_c for short bubbles is driven by the increasing release of surface energy as the bubble lengthens until the broadened bubble fills the length of the expansion, whereas the resistance of the bubble to flow remains very low as discussed above (see figure 3). Hence, a larger dimensionless flow rate is required to untrap short bubbles as their length increases. Once the trapped bubble exceeds the length of the expansion, the resistance to flow increases with initial bubble length more strongly than the surface energy decreases, as the deformation into the expansion remains broadly similar. Hence, the most stable bubble is always the smallest bubble to fill the length of the expansion when trapped.

The values of Ca_c are approximately of an order of magnitude larger for $Bo = 1.06$ than for $Bo = 0.016$. This is because the presence of buoyancy alters the bubble configuration and enables it to lift off from the bottom boundary of the tube for $Bo \simeq 1$. Hence, the trapped bubble obstructs a smaller fraction of the cross-section of the tube, creating less resistance to the outer constant-flux flow. At $Bo = 1.06$, a larger value of L is required compared with $Bo = 0.016$. This is because the expansion of a bubble into a wider channel is also accompanied a small vertical expansion of the bubble in the presence of buoyancy forces (de Lózar *et al.* 2008). The results are summarized in table 1.

The extent to which the bubble enters the expansion, and thus the reduction in surface energy upon trapping, is strongly dependent on the length of the expansion relative to the width of the tube, l/w. We were able to trap bubbles for $l/w = 0.5$ and $l/w = 2$, as shown in figure 7. The most stable bubble remained the shortest bubble to fill the expansion, implying an approximately linear variation of $(L/w)_{max}$ with l/w. The trapped bubble configuration is one of minimal surface area, or equivalently, of minimum constant curvature, where the bubble is unconfined in the limit of small Ca. A bubble whose main body is much longer than its end caps, enters the expansion approximately with the curvature, $(1/l + 1/b)$, while its end caps inside the channel have the curvature of $(1/w + 1/b)$. As evident in figure 7, when the expansion length
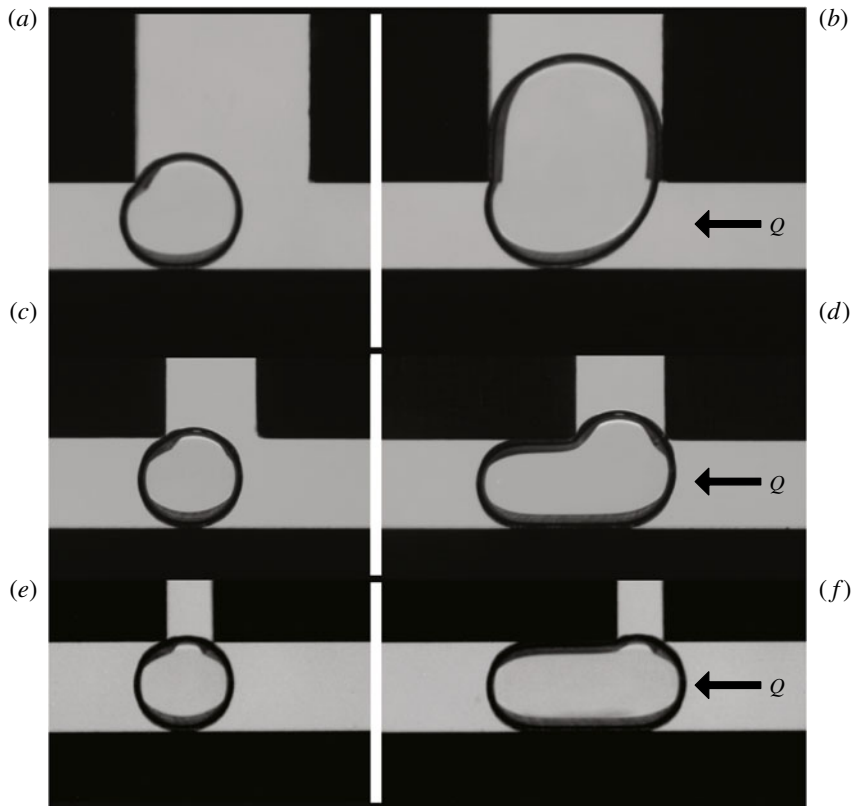
FIGURE 7. Snapshots of bubbles trapped in expansions of different lengths in the millimetric channel, where $w = 3.0$ mm. Top: $l/w = 2.0$, (a) $L/w = 1.68$, $Ca_c = 1.1 \times 10^{-3}$ and (b) $L/w = 4.06$, $Ca_c = 1.1 \times 10^{-3}$. Middle: $l/w = 1.0$, (c) $L/w = 1.25$, $Ca_c = 0.46 \times 10^{-3}$ and (d) $L/w = 2.56$, $Ca_c = 0.34 \times 10^{-3}$. Bottom: $l/w = 0.5$, (e) $L/w = 1.18$, $Ca_c = 0.19 \times 10^{-3}$ and (f) $L/w = 2.31$, $Ca_c = 0.09 \times 10^{-3}$.

matched the channel width ($l/w = 1$), the bubble curvature inside the expansion was roughly the same as that of the bubble end caps. At $l/w = 0.5$, the bubble was not able to enter fully into the expansion while maintaining the lower curvature of $(1/w + 1/b)$; thus, broadening into the expansion was not energetically favourable. Consequently, bubbles tended to get trapped at lower values of Ca_c and $(L/w)_{max}$ was reduced compared with $l/w = 1$. However, for $l/w = 2$, the bubble broadened significantly, as the bubble curvature inside the expansion was lower. Therefore, the measured values of Ca_c were larger than for $l/w = 1$ and $(L/w)_{max}$ increased. The bubble could even be driven entirely into the expansion as Ca was reduced, provided that the expansion was sufficiently deep to accommodate the volume of the bubble. This enabled the trapping of long bubbles at the maximum value of Ca_c irrespective of their length.

4. Static model of a trapped bubble

As discussed in § 3, the trapping and release of a bubble is governed by two physical ingredients: gradient in bubble surface energy and pressure force imposed by the external fluid flow. This idea is summarized into a simple criterion for a bubble

release whereby the work of the pressure forces over the length of the expansion must exceed the surface energy required for the trapped bubble to reenter the tube of square cross-section. If ΔS denotes the increase in surface area from the trapped to the released bubble, F_p the net pressure force on the bubble due to the external flow, and y the axial flow direction, this criterion can be expressed as

$$\sigma \, \Delta S \lesssim \int_{l/2} F_p(y) \, \mathrm{d}y, \qquad (4.1)$$

where $l/2$ is the distance over which the pressure forces must work to push the broadest part of the bubble back into the square tube. If we non-dimensionalize ΔS with lb, F_p with $\mu Q/w$ and y with l, equation (4.1) can be rearranged to yield $Ca_c \sim \Delta S^* / \int_{1/2} F_{p,c}^* \, \mathrm{d}y^*$, where $F_{p,c}^*$ is now the critical dimensionless pressure force needed to release the bubble.

In order to verify the validity of (4.1), we need accurate estimates of both pressure forces F_p and change in bubble surface area ΔS. The pressure forces can be estimated from the experimental measurements of the pressure drop between the tip and tail of the trapped bubble, but the accurate determination of ΔS requires numerical calculation. For this, we model a capillary static bubble in the expansion subject to body forces of gravity and pressure drag. This formulation requires a simplified pressure distribution in order to implement the effects of the pressure drag on the bubble, whereby the pressure decreases linearly in the streamwise direction as explained in further detail below. As discussed in § 3, for initial bubble lengths $L/w \geqslant 1.8$, the pressure difference actually increases linearly with the length of the main body of the bubble, while the end caps hardly contribute to the pressure drag as shown in figure 3. Hence, the assumption of a linear pressure distribution becomes valid only in the limit of very long bubbles where the main body is much longer than the end caps. However, a more accurate pressure distribution would require the solution of the complete three-dimensional free-boundary Stokes flow problem, whose numerical simulation is hampered by very low values of Ca, associated with thinning liquid films. The three-dimensional finite-element simulations of de Lózar *et al.* (2008) describe bubble motion in square tubes for capillary numbers based on bubble speed down to 10^{-3}, while the typical dimensionless flow rates thresholds in the trapping geometry are in the range $10^{-5} < Ca_c < 10^{-3}$ (see figure 6). Appropriate numerical approaches to this problem include quasi-static simulations (Jensen, Stone & Bruus 2006) and boundary integral methods (Janssen & Anderson 2008).

In order to calculate static bubble shapes, we used the readily available numerical tool, Surface Evolver (Brakke 2008), which is an optimization software that minimizes the total energy of a user-defined surface under given constraints. Designed for a static system, it can incorporate any type of energy (e.g. surface tension, gravity) that can be expressed in terms of a surface integral. Thus, we were able to implement the effect of a constant pressure gradient on the bubble as a bubble energy, analogously to the effect of gravity.

For simplicity, we hereby define the channel geometry with a single dimensional length scale, W, to represent the channel depth b, width w, and the length of the expansion l. The width d of the expansion (see figure 1) does not come into play, as we consider the limit in which the bubble never touches the bottom of the expansion. In addition to the axial direction, y, the dimensional lateral and vertical directions are denoted as x and z, respectively. Dimensional energies in the system are denoted as E with appropriate subscripts. Dimensionless variables are starred and based on the

following scales:

$$E^* = E/(\sigma W^2), \quad (x^*, y^*, z^*) = (x, y, z)/W, \quad (4.2)$$

where σW^2 is the characteristic surface energy in the system. Furthermore, the dimensionless channel length scale W^* is set to be one in all of the simulations.

Apart from the surface energy of the bubble, another relevant energy in our problem is the gravitational potential. Although the gravitational term is not explicitly shown in (4.1), both ΔS^* and F_p^* are strongly dependent on the relative strength of gravity. In particular, at a fixed flow rate, the resultant magnitude of F_p^* depends strongly on the Bond number *Bo*, as the higher value of *Bo* leads to the bubble lifting off the bottom wall of the channel, hence, allowing more fluid to pass underneath; this subsequently reduces the pressure buildup, compared with the smaller *Bo* case. The gravitational energy E_g^* can be expressed as

$$E_g^* = G \iiint_{V_{bubble}^*} z^* \, \mathrm{d}V^*, \quad (4.3)$$

or, equivalently, by the divergence theorem,

$$E_g^* = G \iint_{S_{bubble}^*} \frac{z^{*2}}{2} \boldsymbol{n} \cdot \mathrm{d}\boldsymbol{A}^*, \quad (4.4)$$

where $G = 4Bo = \rho g W^2/\sigma$, and *Bo* is now defined with W instead of b. We set $G = 4.24$ and 0.06 to match the experimental parameters in the millimetric and micrometric tubes, respectively.

In order to implement the effects of the pressure drag on the bubble, pressure was assumed to decrease linearly in the y^*-direction, which can be expressed as an energy in the following surface integral form,

$$E_p^* = -\phi \iint_{S_{bubble}^*} \frac{y^{*2}}{2} \boldsymbol{n} \cdot dA^*, \quad (4.5)$$

where the dimensionless constant $\phi \equiv |\nabla P| W^2/\sigma$ is the ratio of pressure build-up to surface tension effects. In the capillary static model, the pressure gradient was uniform so that $|\nabla P| \propto Q$ and hence $\phi \propto Ca$. This is a good approximation of the experimental pressure distribution $\Delta P/(L - L_0) \propto Ca$ shown in figure 3 on the limit of long bubbles.

We chose the initial configuration to be a hexagonal bubble of volume V_{bubble}^* positioned at a distance d_i^* from the backward-facing step, as shown in figure 8(a). The bubble surface was constrained by the channel walls on all sides, except for the case of $G = 4.24$ in which the bubble never touched the channel bottom at $z^* = -W^*/2$ due to buoyancy. In addition, at the expansion located between $y^* = [-W^*/2, W^*/2]$ at $x^* = W^*/2$, the bubble was unconstrained in the x^*-direction and was allowed to relax its shape into the expansion. Surface Evolver uses a finite-element method, in which the surface is represented as a set of triangles that are defined in terms of vertices, edges and facets. While obeying the constraints, the Surface Evolver iteratively calculates the gradient of total energy at each location and moves the vertex in the direction that reduces the energy by a gradient descent method. In our simulation, during the iterative step, the surface was also routinely refined by subdividing the triangles, while facets whose area was less than a tolerance value were deleted for best results. In addition to the gradient descent method, we also
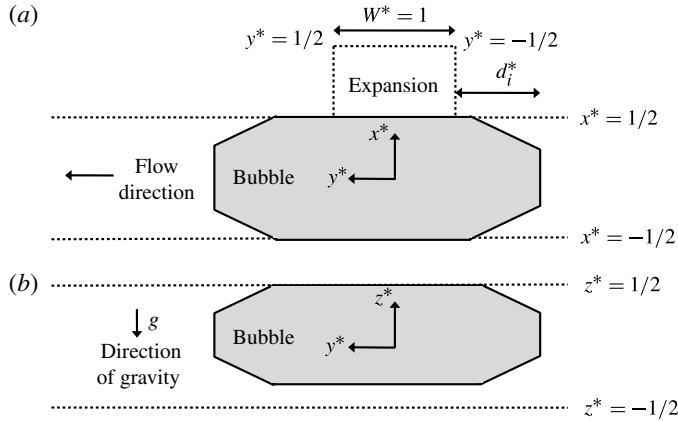
FIGURE 8. Initial bubble configuration used in the Surface Evolver calculations: the origin of the $x^*y^*z^*$ axes is set at the centre of the channel, with respect to the expansion location. The channel is a square capillary with scaled width $W^* = 1$, and the expansion length is also taken to be $W^* = 1$. (a) On the x^*–y^* plane, the initial rectangular bubble is stationed at a distance d_i^* from the backward-facing step. (b) On the y^*–z^* plane, for the case of $G = 4.24$, the bubble is set to not touch the channel bottom at $z = -W^*/2$.

employed the Hessian minimization step when the surface was assumed to be close to convergence. This method computes the second derivative of energy (i.e. Hessian) at each vertex and moves the vertices in a way that allows the Hessian to go to zero. Thus, at given values of G and ϕ, we evolved the bubble surface via the gradient descent method, surface refinement and Hessian minimization, until an equilibrium solution was reached when the change in computed surface area became less than 10^{-6}. Surface Evolver calculations of static bubbles in the expansion were run for increasing values of the flow pressure gradient ϕ (increment of 0.01), at constant G, until a critical value ϕ_c was reached, beyond which a static solution could not be found, i.e. the convergence criterion was not reached.

Because we omitted to calculate the flow conditions that lead to trapping by not solving the Stokes flow variational problem, our formulation does not incorporate a selection criterion. Hence, we obtained multiple static bubble solutions for set values of G and ϕ, depending on the initial bubble configuration. This is illustrated in figure 9, where the variation of ϕ_c with initial bubble length is shown for different values of d_i^* in the range $0 \leqslant d_i^* \leqslant 0.5$. The curves obtained for increasing values of d_i^* are shifted vertically towards higher values of ϕ_c, but the variation of ϕ_c with L/w is similar in each case, suggesting the existence of a continuous family of static solutions.

In order to differentiate between different bubble shapes, we parametrized the top-view bubble projection in terms of three dimensionless quantities: the distances d_c^* and d_e^* defined in figure 10 corresponding to the maximum intrusion of the bubble into the channel upstream of the backward-facing step and into the expansion, respectively, and the length of the trapped bubble L_t/w. The variation of the experimental values of d_c^* and d_e^* with initial bubble length L/w is shown in figure 10. These parameters vary for short bubbles, but reach constant values for long bubbles (i.e. bubbles that fill the entire length of the expansion), indicating that the experimental flow systematically selects same type of bubble, for both $Bo = 1.06$ and $Bo = 0.016$. By injecting the air bubble into the system through the expansion rather than it being
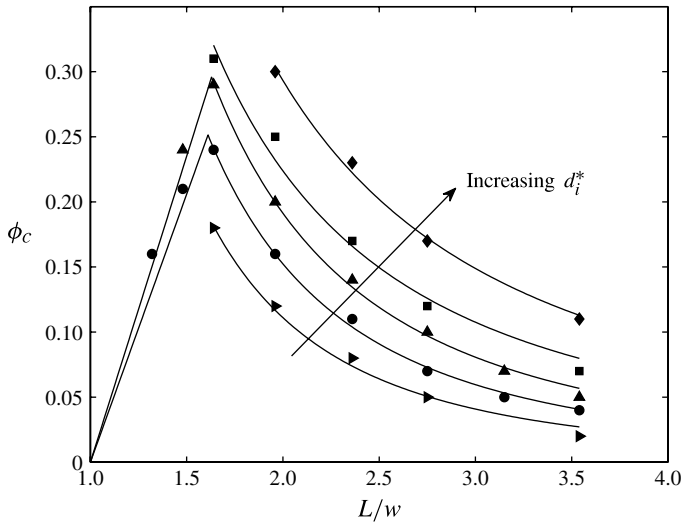
FIGURE 9. Dependence of ϕ_c on initial bubble length L/w for different values of d_i^* (see figure 8 for a definition of d_i^*): $d_i^* = 0$ (►), $d_i^* = 0.1$(●), $d_i^* = 0.2$ (▲), $d_i^* = 0.3$ (■) and $d_i^* = 0.5$ (◆). The solid lines are plotted to guide the eye.

transported by the flow down the main tube, we were also able to select different types of trapped bubbles and, hence, support the numerical findings of multiple trapped bubble solutions. In order to select static bubbles whose top-view projection matches the critical shapes of trapped bubbles observed experimentally, we chose an initial condition $d_i^* \simeq d_c^*$, i.e. $d_i^* = 0.10$ for $Bo = 1.06$ and $d_i^* = 0.16$ for $Bo = 0.016$. We were able to accurately match short bubbles with this initial condition, but for long bubbles, it led to the stochastic selection of two types of bubbles: one that matched the experimental bubbles closely and another shorter trapped bubble that intruded significantly further into the expansion. The closely matched bubbles also had similar trapped lengths, which were approximately proportional to the initial bubble length L/w as shown in figure 11. However, both types of bubbles detached from the backward-facing step of the expansion at a similar value of ϕ_c to within 0.01. We selected the closely matched bubbles for further analysis.

In figure 12, we show a qualitative comparison between the values of ϕ_c, our numerical measure of dimensionless flow rate, and the experimentally obtained values of Ca_c, as a function of initial bubble length, L/w. A constant factor Γ is applied to rescale ϕ_c onto Ca_c based on the longest bubble investigated. Typical matched bubble shapes obtained with Surface Evolver are shown similarly to the experimental bubble shapes in figure 6. Despite the significant approximations made to the pressure distribution around the bubble in the model, the numerical results exhibit a trapping threshold that depends on the initial bubble length qualitatively similarly to the experimental results. In both cases, the variation of the surface energy release dominates over the change in pressure drag for short bubbles, hence resulting in a steep increase of the critical value ϕ_c for trapping. However, for long bubbles, the change in surface energy release with initial bubble length is small while the pressure drag increases significantly, leading to a decrease in ϕ_c. As in figure 6, the length of the most stable bubble was estimated by finding the intersection of a linear interpolation for small bubbles, with a power fit of the form $L/w = A Ca_c^B$ for larger
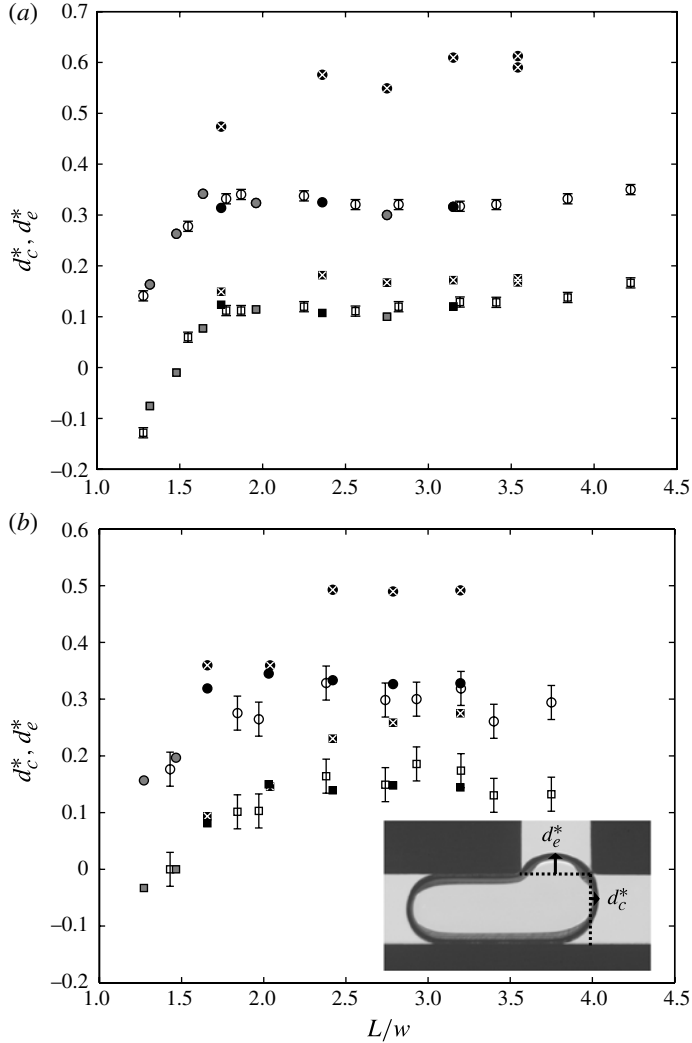
FIGURE 10. Comparison between experimental (empty symbols) and numerical (solid symbols) bubble shapes at threshold. The bubble shapes are parametrized by d_c^* (squares) and d_e^* (circles), the intrusion distance into the channel upstream of the expansion and into the expansion, respectively (see the inset). (*a*) Millimetric tube with $d_i^* = 0.10$ and $G = 4.24$. (*b*) Micrometric tube with $d_i^* = 0.16$ and $G = 0.06$. Black symbols correspond to matching bubbles obtained by solely imposing the value of d_i^*, symbols with a white cross denote non-matching bubbles obtained with this initial condition and grey symbols correspond to matching bubbles selected by additionally imposing a maximum intrusion distance into the expansion.

bubbles (solid line). We obtained $(L/w)_{max} = 1.61 \pm 0.04$ and $(L/w)_{max} = 1.48 \pm 0.08$ for the Surface Evolver calculations at $Bo = 1.06$ and $Bo = 0.016$, respectively, compared with the experimentally obtained values $(L/w)_{max} = 1.71 \pm 0.08$ and $(L/w)_{max} = 1.52 \pm 0.14$.

The scaling factor Γ depends on the initial bubble length, but it can be estimated analytically in the limit of very long bubbles, whose main body is much longer its end
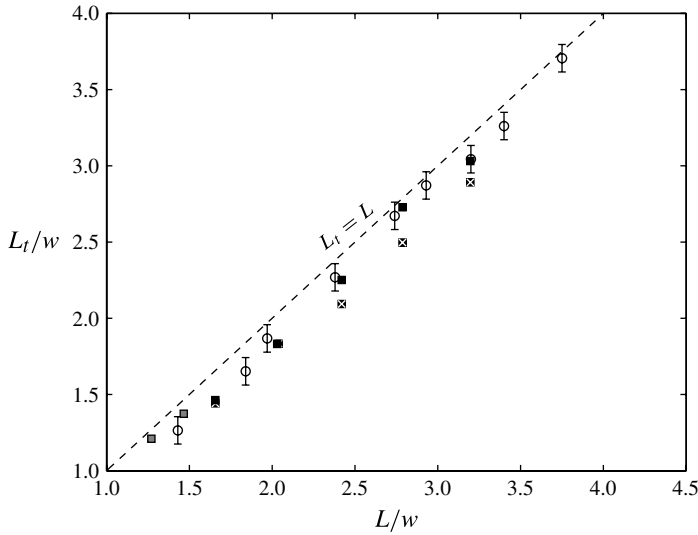
FIGURE 11. Variation of the length of the trapped bubble L_t/w with initial bubble length L/w in the micrometric tube ($G = 0.06$). See figure 10 for legend.

caps in the absence of gravity forces. At $Bo = 0.016$, a very long bubble is expected to occupy most of the square channel, except for four corners of the channel. The total cross-sectional area occupied by the bubble can be expressed as mW^2, where m is the wet fraction and W^2 the channel cross-sectional area. In the case of a steadily moving bubble inside a square tube at $Bo = 0$, de Lózar *et al.* (2008) found numerically that $m \simeq 0.07$ for $Ca \simeq 10^{-3}$, with only a very weak dependence of m on Ca for $Ca < 10^{-3}$. If the geometry of the very long bubble is known by assuming a value of m, one can estimate the pressure gradient due to the flow around the bubble, based on the calculations by Ransohoff & Radke (1988). They calculated the flow of a wetting fluid inside non-circular capillaries, when the channel is occluded by an inviscid bubble and all of the fluid is assumed to go through the corners formed around it. In particular, the solution was found valid in the limit of small Bond, Reynolds and capillary numbers, when the axial variation of the bubble curvature can be neglected. Thus, this coincides with the flow around a trapped bubble inside the microchannel, when the main body of the bubble is much longer than the end caps. They showed that the dimensional pressure gradient is given by $|\nabla P| = (\beta(4 - \pi)/m^2)(\mu Q/W^4)$, where β is the flow resistance factor calculated numerically for different channel shapes; for a square channel, they found β to be 93.93. Using this expression, the parameter ϕ becomes $\phi = (\beta(4 - \pi)/m^2)Ca$ or, equivalently,

$$Ca_c = \frac{m^2}{\beta(4 - \pi)}\phi_c. \tag{4.6}$$

valid only in the low Bo case. Specifically, in order for the prefactor to match the value $\Gamma = 6.3 \times 10^{-5}$ obtained from the data shown in figure 12(*b*), we find $m = 0.071$, which is in close agreement with the wet fraction predicted by de Lózar *et al.* (2008). Moreover, the proportionality coefficient between dimensionless pressure gradient and Ca, $\beta(4 - \pi)/m^2 \simeq 1.6 \times 10^4$, is consistent with the value of
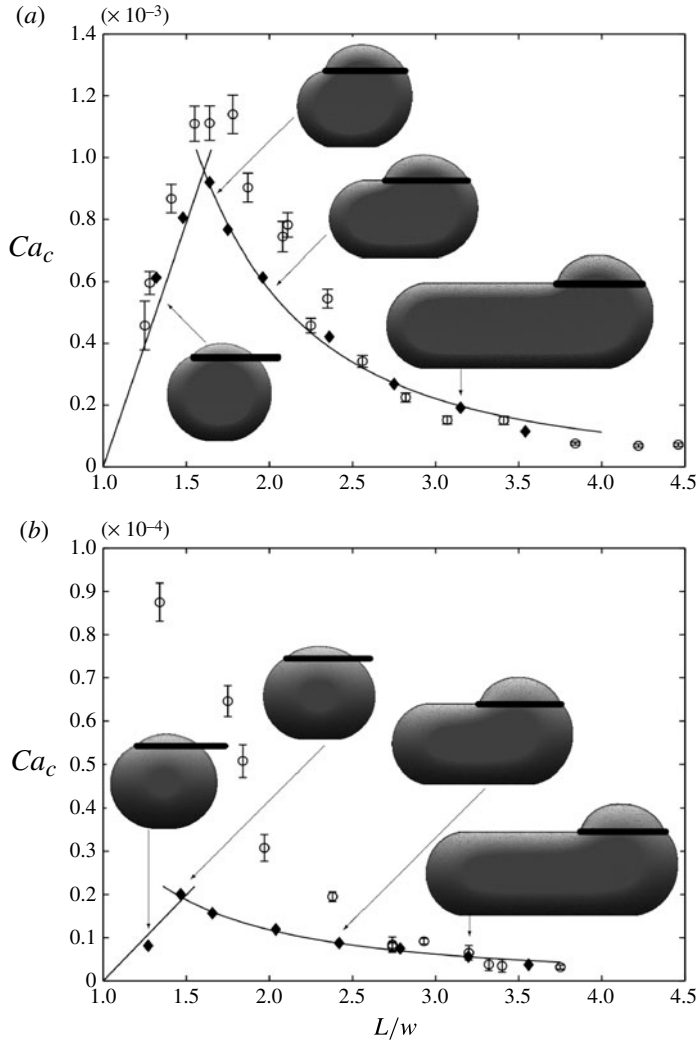
FIGURE 12. Comparison of ϕ_c ($\blacklozenge$) (scaled by a constant factor Γ to match Ca_c for the longest calculated bubbles) with the experimentally obtained values of Ca_c ($\bigcirc$) as a function of initial bubble length, L/w. Typical bubble shapes obtained with Surface Evolver are shown similarly to the experimental bubble shapes in figure 6. As in figure 6, the length of the most stable bubble was estimated by finding the intersection of a linear interpolation for small bubbles, with a power fit of the form $L/w = ECa_c^F$ for larger bubbles (solid line). (*a*) Millimetric tube: $G = 4.24$, $w = 3.0$ mm, $L = 3.0$ mm and $\Gamma = 3.8 \times 10^{-3}$ where $(L/w)_{max} = 1.61 \pm 0.04$ for the surface evolver calculations compared with the experimentally obtained $(L/w)_{max} = 1.71 \pm 0.08$. (*b*) Micrometric tube: $G = 0.06$, $w = 0.25$ mm, $l = 0.25$ mm and $\Gamma = 6.3 \times 10^{-5}$ where $(L/w)_{max} = 1.48 \pm 0.08$ for the surface evolver calculations compared with the experimentally obtained $(L/w)_{max} = 1.52 \pm 0.14$.

$\alpha = (1.9 \pm 0.2) \times 10^4$ obtained experimentally in figure 3, especially considering the limited set of pressure data available for bubbles longer than $L/w \geqslant 2.4$.
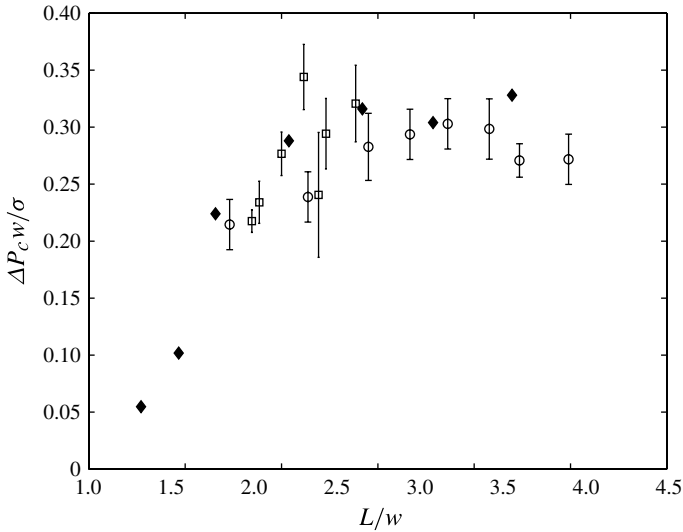
FIGURE 13. Comparison between critical pressure differences of release (non-dimensionalized on the capillary scale σ/w) measured experimentally (open symbols) and determined using the release criterion given in (4.1) from the change in surface energy of experimentally matched bubble shapes calculated with Surface Evolver ($\blacklozenge$). The experimental pressure measurements were made in the microtube where $w = 0.25$ mm: ($\square$) critical pressure difference determined from using the value of Ca_c and the measured proportionality coefficient with Ca; ($\bigcirc$) direct measurements performed for values of the dimensionless flow rate 10 % below Ca_c, and extrapolated to a threshold value using the measured relationship $\Delta Pw/\sigma = \alpha Ca(L - L_0)/w$.

5. Bubble release criterion

The pressure forces are approximated to $F_p \simeq \Delta Pwb$, where ΔP is the pressure difference between the tail and the tip of the bubble. Hence, the release criterion given in (4.1) yields a pressure difference at the trapping threshold that is proportional to the increase in surface area of the bubble required to untrap the bubble:

$$\Delta P_c \simeq \frac{2\sigma \Delta S}{l w b}, \tag{5.1}$$

if the variation in pressure force during the release process is neglected.

In order to evaluate this bubble release criterion, we compared the critical pressure difference of release measured experimentally in the microtube to that evaluated using the change in surface energy of experimentally matched bubble shapes calculated with Surface Evolver. We measured the critical pressure of release (figure 13) using two techniques. The first was to determine the critical pressure difference from the value of Ca_c and the measured proportionality coefficient with Ca; the second involved direct measurements performed for values of the dimensionless flow rate 10 % below Ca_c, which were then extrapolated to a threshold value using the measured relationship $\Delta Pw/\sigma = \alpha Ca(L - L_0)/w$ (see figure 2). This latter method enabled the evaluation of the critical pressure difference in longer bubbles up to $L/w = 3.5$.

The good agreement between the direct experimental measurements and the Surface Evolver results suggests that the release criterion proposed in (4.1) provides a good measure of the trapping threshold in this system, as long as the flow selects a unique

family of trapped bubbles. It also suggests that heat losses from viscous frictional energy are minimal in our setup, despite the thin liquid films associated with the trapped bubble configuration. Independent estimation of the rate of change of frictional energy yields values of less than 1 % of the rate of change of surface energy. All the measurements are for long trapped bubbles, i.e. bubbles that fill the entire length of the expansion. For $L/w \lesssim 2.4$, the pressure force required to release the bubble increases with L/w, indicating an increase in the surface energy deficit, and thus, the development of the expanded region as the bubble lengthens. For $L/w \gtrsim 2.4$, the pressure difference reaches a constant critical value, which means that the expanded region of the trapped bubble does not further change with initial bubble length, so that the trapped bubble grows solely by lengthening its main body. As flow rates depend on the gradient of pressure ∇P, instead of the pressure difference ΔP, this suggests that the dimensionless critical flow rate, Ca_c, must scale as $(L/w)^{-1}$, in this long bubble limit. This result is analogous to the findings of Dangla *et al.* (2011) in the case of a large 'pancake' droplet of radius R inside a Hele-Shaw cell. They show that the gradient in surface energy is independent of the drop radius, while the drag force is proportional to R^2, the surface area of the two-dimensional drop, so that the critical Ca of untrapping scales as $1/R^2$.

6. Conclusion

We have studied bubble trapping phenomena under constant-flux flow in tubes of square cross-section that include a sudden streamwise expansion, which is formed by a pair of backward and forward-facing steps. A bubble of finite volume, and of an initial length L greater than the width of the tube ($L/w > 1$), can become trapped because it releases surface energy upon broadening into the expansion, which has to be replaced by the work of the pressure forces in order for the bubble to be forced back into the tube. The broadening of the bubble into the expansion is accompanied by critical slowing down of its tip as the trapping threshold is approached, suggesting that the trapped bubble is released through loss of stability. The gradients in surface energy generated by the broadening of the bubble into the expansion depend strongly on its length, with minimal entry when $l/w = 0.5$ while long bubbles can enter the expansion fully for $l/w = 2.0$ because of the favourable reduction in mean curvature of the bubble.

The most stable bubbles are relatively short and their length is approximately linearly dependent on that the expansion. For short pores with $l/w \leqslant 1$, the lengthening of a trapped bubble through coalescence will dislodge it, while for $l/w = 2$, any additional volume will be absorbed into the pore provided if it is deep enough, so the bubble may remain trapped. The maximum value of Ca_c is an order of magnitude larger for $Bo = 1.06$ than for $Bo = 0.016$ because of the influence of buoyancy on the cross-sectional configuration of the trapped bubble, which controls the magnitude of the pressure drag on the bubble.

Despite the simplicity of our geometry, the presence of thin liquid films render numerical models of trapping both challenging and computationally intensive. Instead, we have verified that a bubble is released if the work of the pressure forces over the length of the expansion exceeds the surface energy required for the trapped bubble to reenter the tube of square cross-section. We obtain good agreement between direct measurements of the pressure drop between tail and tip of the trapped bubble and the pressure drop estimated from the change in bubble surface energy calculated with a capillary static model, where the capillary static bubble is subject to body forces of

gravity and pressure drag. This simple model yields static bubble solutions that can be matched closely to the experimental bubbles at the trapping threshold for carefully selected initial conditions. Whereas the dynamics of the trapping process select a unique type of trapped bubble, there is evidence of a broad range of static bubble solutions, some of which have also been observed experimentally when altering the initial conditions for trapping. A variety of trapped bubble configurations may occur in practice, depending on geometry and flow conditions.

Where trapped bubbles are to be avoided, streamwise expansions ought to have lengths or depths smaller than the width of the channel, while bubbles/droplets smaller than the tube width or relatively long will preferentially escape. Hence, minimal trapping may be expected in porous networks where the pore/pore throat ratio is small, such as sandstone, while large bubbles will escape most effectively from fibre reinforcements during the manufacturing of composites. In lab-on-a-chip applications where trapping of droplets for manipulation is desirable, our study provides general guidelines for the stability of droplets subject to viscous and surface tension forces, although the effect of surfactants routinely added to reduce the interaction of droplets with the channel may need to be accounted for.

Acknowledgements

Supplementary movies

Supplementary movies are available at http://dx.doi.org/10.1017/jfm.2013.103.

REFERENCES

ABBYAD, P., DANGLA, R., ALEXANDROU, A. & BAROUD, C. N. 2011 Rails and anchors: guiding and trapping droplet microreactors in two dimensions. *Lab on a Chip* **11**, 813–821.

AHN, B., LEE, K., LEE, H., PANCHAPAKESAN, R. & OH, K. W. 2011 Parallel synchronization of two trains of droplets using a railroad-like channel network. *Lab on a Chip* **11**, 3956–3962.

AMYOT, O. & PLOURABOUÉ, F. 2007 Capillary pinching in a pinched microchannel. *Phys. Fluids* **19**, 033101.

BOUKELLAL, H., SELIMOVIC, S., JIA, Y., CRISTOBAL, G. & FRADEN, S. 2009 Simple, robust storage of drops and fluids in a microfluidic device. *Lab on a Chip* **9**, 331–338.

BRAKKE, K. 2008 Surface Evolver manual. http://www.susqu.edu/facstaff/b/brakke/evolver/evolver.html.

CHIO, H., JENSEN, M. J., WANG, X., BRUUS, H. & ATTINGER, D. 2006 Transient pressure drops of gas bubbles passing through liquid-filled microchannel contractions: an experimental study. *J. Micromech. Microengng* **16**, 143–149.

DANGLA, R., LEE, S. & BAROUD, C. N. 2011 Trapping microfluidic drops in wells of surface energy. *Phys. Rev. Lett.* **107**, 124501.

GU, H., MURADE, C. U., DUITS, M. H. G. & MUGELE, F. 2011 A microfluidic platform for on-demand formation and merging of microdroplets using electric control. *Biomicrofluidics* **5** (1), 011101.

HAZEL, A. L. & HEIL, M. 2002 The steady propagation of a semi-infinite a semi-infinite bubble into a tube of elliptical or rectangular cross-section. *J. Fluid Mech.* **470**, 91–114.

HE, M., KUO, J. S. & CHIU, D. T. 2005 Electro-generation of single femtoliter- and picoliter-volume aqueous droplets in microfluidic systems. *Appl. Phys. Lett.* **87** (3), 031916.

JANSSEN, P. J. A. & ANDERSON, P. D. 2008 A boundary-integral model for drop deformation between two parallel plates with non-unit viscosity ratio drops. *J. Comp. Phys.* **227**, 8807–8819.

JENSEN, M. J., GORANOVI, G. & BRUUS, H. 2004 The clogging pressure of bubbles in hydrophilic microchannel contractions. *J. Micromech. Microengng* **14**, 876–883.

JENSEN, M. J., STONE, H. A. & BRUUS, H. 2006 A numerical study of two-phase Stokes flow in an axisymmetric flow-focusing device. *Phys. Fluids* **18**, 077103.

KÖHLER, J. M., HENKEL, T., GRODRIAN, A., KIRNER, T., ROTH, M., MARTIN, K. & METZE, J. 2004 Digital reaction technology by micro segmented flow-components, concepts and applications. *Chem. Engng J.* **101**, 201–216.

LEGAIT, B. 1983 Laminar flow of two phases through a capillary tube with variable square cross section. *J. Colloid Interface Sci.* **96**, 28–38.

DE LÓZAR, A., HEAP, A., BOX, F., HAZEL, A. L. & JUEL, A. 2009 Partially-occluded tubes can force switch-like transitions in the behaviour of propagating bubbles. *Phys. Fluids* **21**, 101702.

DE LÓZAR, A., JUEL, A. & HAZEL, A. L. 2008 The steady propagation of an air finger into a rectangular tube. *J. Fluid Mech.* **614**, 173–195.

LUNDSTRÖM, T. S. 1996 Bubble transport through constricted capillary tubes with application to resin transfer molding. *Polym. Compos.* **17**, 770–779.

PAILHA, M., HAZEL, A. L., GLENDINNING, P. A. & JUEL, A. 2012 Oscillatory bubbles induced by geometric constraint. *Phys. Fluids* **24**, 021702.

RANSOHOFF, T. C. & RADKE, C. J. 1988 Laminar flow of a wetting liquid along the corners of a predominantly gas-occupied noncircular pore. *J. Colloid Interface Sci.* **121** (2), 392–401.

RENVOISÉ, P., BUSH, J. W. M., PRAKASH, M. & QUÉRÉ, D. 2009 Drop propulsion in tapered tubes. *Europhys. Lett.* **86**, 64003.

TAN, Y.-C., FISHER, J. S., LEE, A. I., CRISTINI, V. & LEE, A. P. 2004 Design of microfluidic channel geometries for the control of droplet volume, chemical concentration, and sorting. *Lab on a Chip* **4**, 292–298.

UM, E. & PARK, J.-K. 2009 A microfluidic abacus channel for controlling the addition of droplets. *Lab on a Chip* **9**, 207–212.

WONG, H., RADKE, C. J. & MORRIS, S. 1995a The motion of long bubbles in polygonal capillaries. Part 1. Thin films. *J. Fluid Mech.* **292**, 71–94.

WONG, H., RADKE, C. J. & MORRIS, S. 1995b The motion of long bubbles in polygonal capillaries. Part 2. Drag, fluid pressure and fluid flow. *J. Fluid Mech.* **292**, 95–110.

XU, J. & ATTINGER, D. 2008 Drop on demand in a microfluidic chip. *J. Micromech. Microeng.* **18** (6), 065020.